A novel Al-Si-Ni-Fe near-eutectic alloy for elevated temperature applications

Qing Cai, Changming Fang, Ewan Lordan, Yun Wang, Isaac T.H. Chang [*], Brian Cantor

Brunel Centre for Advanced Solidification Technology (BCAST), Brunel University London, Uxbridge UB8 3PH, UK

ABSTRACT

A novel near-eutectic Al-15.0Si-4.1Ni-1.9Fe (wt%) alloy with a ternary eutectic reaction of Liquid→α-Al+Si+(Al, Si)$_5$(Fe,Ni) was investigated. Eutectic Si and (Al,Si)$_5$(Fe,Ni) phases exhibit short nanoscale fibrous morphologies with volume fractions of $14.3 \pm 1.6\%$ and $15.1 \pm 1.9\%$, respectively. The (Al,Si)$_5$(Fe,Ni) phase has a tetragonal Al$_{2.7}$FeSi$_{2.3}$-type crystal structure with excellent thermal stability, which contributes to high mechanical properties at room and elevated temperatures. First-principles density-functional theory (DFT) calculations reveal its chemical composition of tetragonal (Al$_{4.75}$Si$_{0.25}$)(Fe$_{0.5}$Ni$_{0.5}$) having Si solution at the Al sites with two Fe neighbours contributes to the lowest solution energy. The newly developed alloy has superior mechanical properties at room and elevated temperatures compared with other typical heat-resistant aluminium alloys, which has great potential for industrial applications.

The development of heat-resistant aluminium alloys has been a continuous subject, which is able to broaden their applications under various working conditions [1,2]. One of their applications is engine components such as pistons and cylinder heads [3–5]. It requires the alloys to have low thermal expansion, high wear resistance, good castability and excellent mechanical properties at elevated temperatures [6]. Currently, most commercial alloys were designed based on binary Al-Si eutectic systems with 11–16% Si, and the addition of some other elements including up to 1.3% Fe, 0.5–5.5% Cu, 0.5–3% Ni, and 0.6–1.3% Mg (wt%) is able to further improve its mechanical performance [3,7,8]. To be detailed, the addition of a large amount of Si contributes to its low thermal expansion, excellent castability and good wear resistance. The addition of Fe and Ni can leads to the formation of interconnected Fe-contained and Ni-contained intermetallic compounds (IMCs), having high thermal stability [9–11]. Besides, Cu and Mg having high solubility in α-Al are able to provide precipitation hardening after ageing. θ'-/θ''-Al$_2$Cu, β'-Mg$_9$Si$_5$/ β''-Mg$_5$Si$_6$ and Q'/Q (AlCuMgSi) precipitates are usually formed in these alloys [12–17]. Nevertheless, these precipitates have limited influence on the mechanical properties of the alloys when exposed to a temperature above 250 °C [15,18–20], due to the high diffusivity and solubility of Cu and Mg in α-Al at elevated temperatures. With respect to increasing the strength of the alloys at elevated temperatures (>250 °C), heat-resistant IMCs play a dominant role [20–22].

Furthermore, it is evident that the unique microstructure and mechanical properties can be achieved in the huge unknown multicomponent phase space [23,24]. Especially, it has bought our attention that multicomponent eutectic alloys with in-situ grown ultrafine IMCs usually have exceptional mechanical or physical properties than binary eutectic counterparts, due to the high volume fraction of IMCs and refined microstructure [25–28]. Hence, exploring Al-Si based multi-component eutectic space and engineering the IMCs is another promising way to further improve mechanical performance at elevated temperatures. In this study, a ternary eutectic reaction in the quaternary Al-Si-Ni-Fe system is found for the first time, and the Al-Si-Ni-Fe near-eutectic alloy is reported. The compressive mechanical properties of the alloy at room and elevated temperatures were investigated, which has been compared with some other commerical aluminium alloys. The relationship between the microstructure and mechanical properties was discussed.

The near-eutectic Al-Si-Ni-Fe alloy (Alloy A) with compositions of Al-15.0Si-4.1Ni-1.9Fe (wt%) was prepared with the pure elements of Si (99.99wt%), Al(99.99wt%), Ni(99.97wt%), and Fe(99.9wt%) by arc melting under pure argon atmosphere. A ~5 g button of the alloy was obtained after arc melting, which was remelted five times to insure the compositional homogeneity. The buttons were processed into ⌀5 mm diameter and 30 mm length rods with a suction casting machine and water-cooled copper mould. For comparison purposes, small buttons
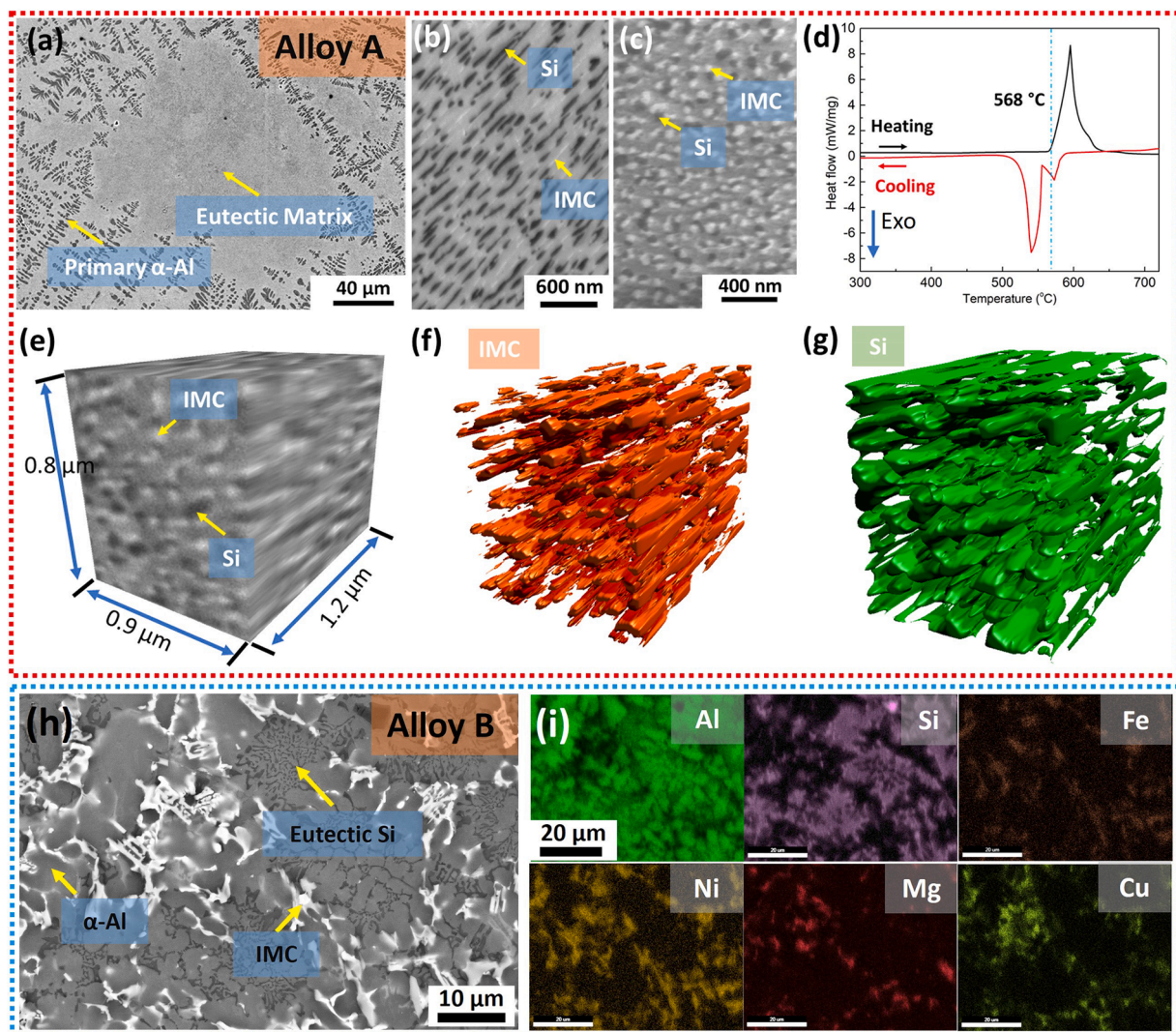
Fig. 1. (a) SEM in-lens image showing the microstructure of Alloy A (b,c) SEM in-lens image under high magnification from different directions of eutectic cells showing Si and intermetallic compound (IMC) (d) DSC heating and cooling curves of Alloy A; the 3D morphology of eutectic phases obtained from FIB-SEM technique (e) 3D structure of α-Al, Si and IMC without segmentation (f) the segmentation of intermetallic compound (IMC) (g) the segmentation of Si; (h) SEM backscattered image of Alloy B (i) SEM EDX mapping of Alloy B.

(~5 g) cut from ingots of a popular commerical aluminium piston alloy with a measured composition of Al-12.8Si-3.9Cu-1.9Ni-1.0Mg-0.4Fe (wt %) [10,29], which is named Alloy B, were also processed into ∅5 × 30 mm rods using the same facility and parameters. The half-length of the rod was cut and cold-mounted. After grinding and polishing, a Zeiss Supra 35 scanning electron microscope (SEM) equipped with energy-dispersive X-ray spectroscopy (EDX) operating at the voltage of 20 kV was used for microstructure characterisation. The size of the eutectic phases was analysed by Image J software. Focused ion beam (FIB) and scanning electron microscope (SEM) technique, which is known as FIB-SEM, was applied for 3D morphology of the eutectic microstructure. The 3D reconstruction of FIB-SEM slides was carried out with Dragonfly software, Version 2020.2 for Windows 10. The nano-/ultrafine eutectic phases were characterised by a JEOL 2100F transmission electron microscope (TEM). TEM samples were prepared by a Gatan Precision Ion Polish system (PIPS) with a voltage of 2–5 kV and milling angles of 3.5–5°. A Netzsh 404F1 differential scanning calorimetry (DSC) was used to measure the melting temperature and heat fusion of the eutectic alloy with a heating and cooling rate of 10 K/min. A Bruker D8 Advance X-ray diffractometer with Cu X-Ray radiation operated at a voltage of 40 kV and a current of 40 mA was used to generate X-ray line profiles for phase identification. The annealing was

carried out with a Carbolite electric resistance furnace. Vickers hardness was obtained with an FM-800 tester with a load of 5 kg and a dwell time of 15 s. The middle part of ∅5 mm rod was sectioned with a length of ~10 mm for the compression test. Uniaxial compression tests were conducted at room temperature, 200 °C, and 300 °C, under a strain rate of 10^{-3} s^{-1}. Nominal stress (force divided by original cross-section area) and nominal strain (cross-head displacement divided by sample length) were obtained. The samples were soaked for 40 min at a designed temperature before the compression test, and the tests were interrupted under elevated temperatures. At least three samples were tested under each temperature. For a better understanding of the formation of IMCs, first-principles density functional theory (DFT) calculations were performed. The detailed method was provided in Supplementary Material.

Figure 1(a) shows the general view of the microstructure of Alloy A. The microstructure consists of the major part of the eutectic matrix and some primary α-Al dendrites. The area fraction of the eutectic region is 92%, indicating the alloy composition close to the eutectic composition. Figure 1(b) and (c) show the detailed microstructure of the eutectic cells from different directions under high magnifications. The SEM images in Fig. 1(b) and (c) reveal three eutectic phases: the grey α-Al, the dark fibrous Si, and the bright fibrous IMC. The fibre lengths of eutectic Si and IMC are less than 1 μm. Figure 1(d) shows the DSC heating and cooling
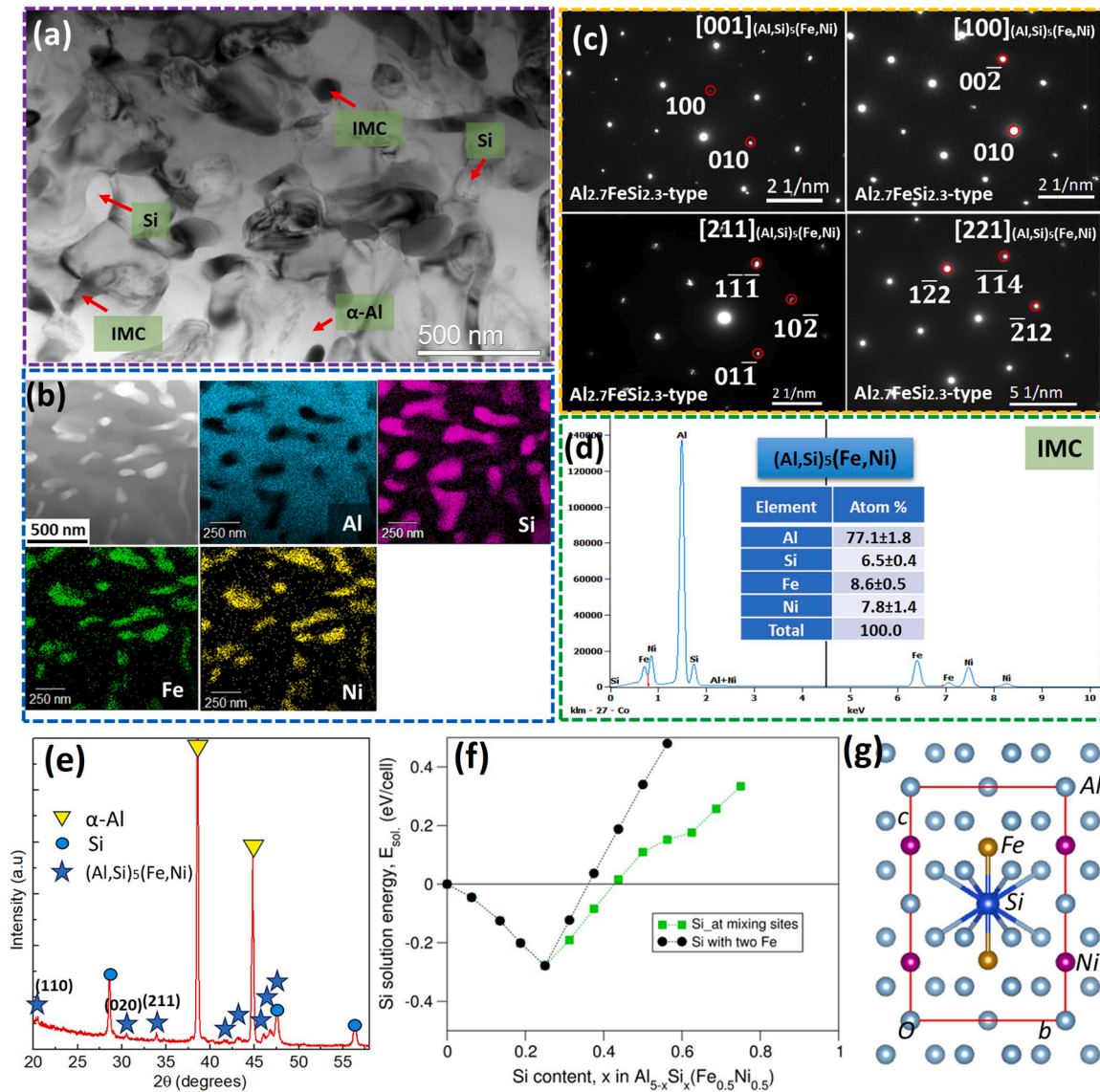
Fig. 2. (a) TEM bright-field image showing the microstructure of eutectic region (b) HAADF-STEM image and element distribution of eutectic phases (c) SADPs of IMC (d) TEM EDX point analysis of IMC; (e) XRD spectra of Alloy A; (f) the Si solution energy on Si contents for the highly stable configurations (g) The schematic structure of the most stable $(Al_{4.75}Si_{0.25})(Fe_{0.5}Ni_{0.5})$.

curves of the alloy, where there is only one endothermic peak with a small shoulder in the heating curve. The main peak and the small shoulder correspond to the melting of the eutectic and the α-Al dendrites, respectively. There is a large exothermic peak with a slightly more separated high-temperature second peak in the cooling curve, corresponding to the solidification of the eutectic and α-Al dendrites, respectively. The 3D morphology of the eutectic structure is shown in Fig. 1(e)–(g). It confirms the fibrous morphology of Si and IMC eutectic phases. The eutectic rod spacing of IMC and Si is measured as 98 ± 32 and 140 ± 40 nm, respectively. The average diameter of the Si fibres is 80 ± 20 nm, while the average diameter of IMC is 82 ± 35 nm. The volume fraction of Si and IMCs are $14.3 \pm 1.6\%$ and $15.1 \pm 1.9\%$, respectively. Figure 1(h) shows a general view of the microstructure of Alloy B. The microstructure consists of the binary eutectic cells (Si+α-Al), small α-Al dendrites and IMCs (bright phases) at eutectic cell boundaries. SEM EDX mapping of Alloy B is shown in Fig. 1(i). It can be found that Si is mainly distributed in the eutectic cells, and IMCs are distributed at cell boundaries having Cu, Ni, Fe and Mg elements. These two alloys were solidified under the same cooling rate. Alloy A has a much finer microstructure than Alloy B, and it indicates that refined

eutectic microstructure can be achieved under multi-component ternary eutectic solidification.

Figure 2(a) shows TEM bright-field image of the microstructure in the eutectic region from Alloy A. The HAADF-STEM image and element distribution of the eutectic phases are shown in Fig. 2(b). From the compositional quantification by the TEM/EDX in Fig. 2(d), the IMC has an average composition of 77.1%Al, 6.5%Si, 8.6%Fe and 7.8%Ni (at.%). Figure 2(c) shows the selected area electron diffraction patterns (SADPs) obtained from 4 different zone axes of the eutectic IMC, which establishes a tetragonal crystal structure for the IMC, with its lattice parameters measured as $a = b = 5.95$ Å, $c = 9.82$ Å, and $\alpha = \beta = \lambda = 90°$. The IMC is therefore very similar to the tetragonal $Al_{2.7}FeSi_{2.3}$ phase, which has $a = b = 6.061$ Å, $c = 9.525$ Å, and $\alpha = \beta = \lambda = 90°$ [30]. Combined with the TEM/EDX results in Fig. 2(d), the structure formula of the IMC is believed to be $(Al,Si)_5(Fe,Ni)$. The XRD spectra is shown in Fig. 2(e), and peaks of $(Al,Si)_5(Fe,Ni)$ phase are identified based on $Al_{2.7}FeSi_{2.3}$ phase from the database.

To obtain insight into the formation and stability of the $(Al,Si)_5(Fe, Ni)$ compounds, first-principles density functional theory method was employed based on the Al_5Fe model [30]. The calculations reveal that Ni
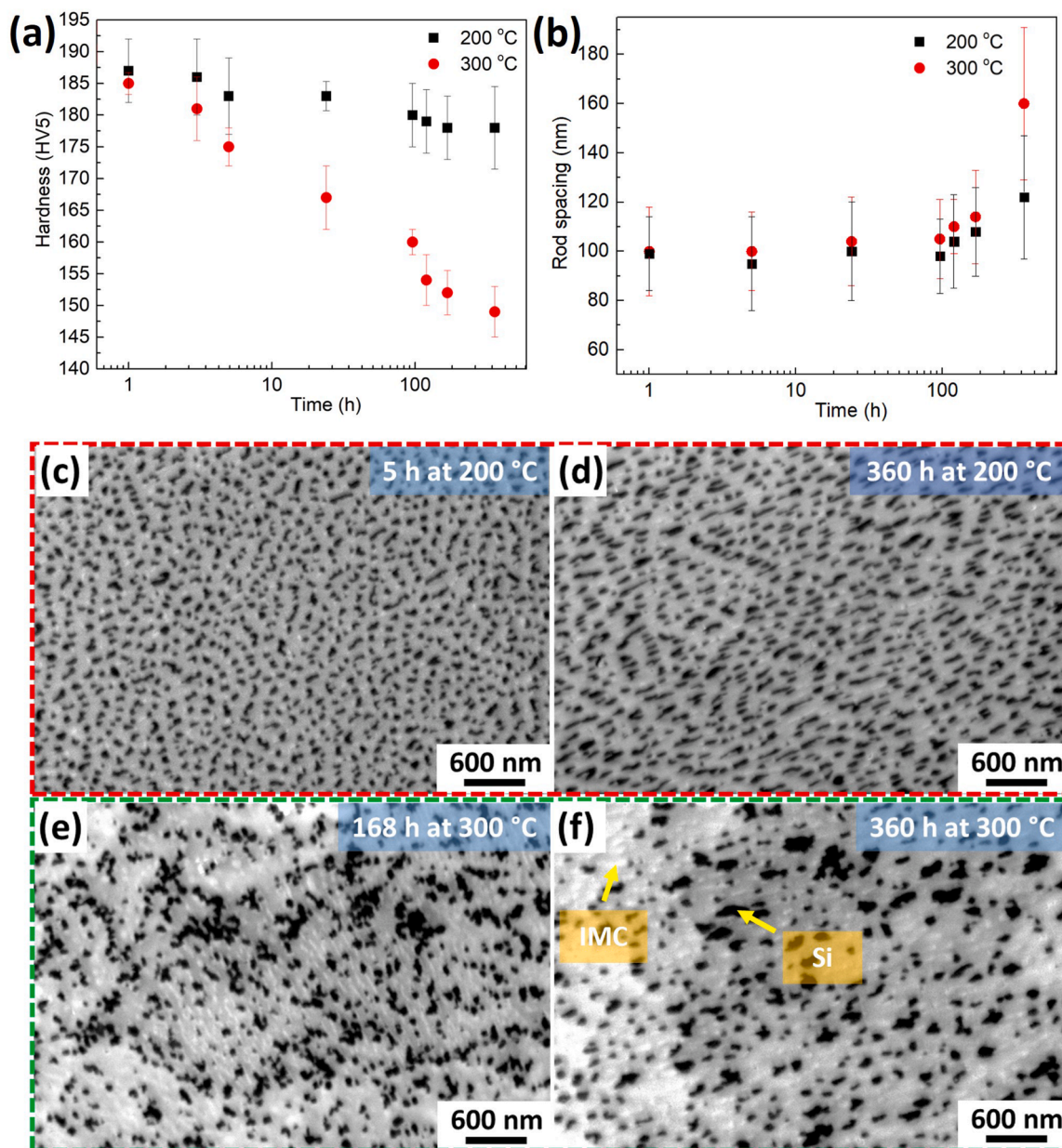
Fig. 3. (a) Vickers hardness of Alloy A after annealing at 200 °C and 300 °C for different times (b) rod spacing of IMC after annealing at 200 °C and 300 °C for different times; SEM in-lens image showing the microstructure of Alloy A after annealing at 200 °C for 5 h (c), after annealing at 200 °C for 360 h (d), after annealing at 300 °C for 168 h (e), and after annealing at 300 °C for 360 h (f).

atoms prefer mixing at the layers parallel to the (c-)-axis. Si prefers the neighbourhood of Fe atoms and no other Si in its neighbourhood. The stable configuration has one Si solutioned at the Al sites with two Fe neighbours, which was used as the starting point. The results of first-principles calculations are summarized in Table S1 (Supplementary Material). Figure 2(f) shows that at low Si content, the highly stable configurations result from the solution of Si at the Al sites with two Fe neighbours (black circles). The solution energy decreases with increasing Si content at the Al sites with two Fe neighbours till Si content reaches $x = 0.25$, which corresponds to the occupation of one-quarter of the Al1 sites [30]. The schematic structure of the highly stable configuration is shown in Fig. 2(g). Further addition of Si causes the solution energy to increase almost linearly with the Si contents. Calculations showed that from the most stable configuration, the energy increase rate is slower for Si solution at the sites with one Fe and one Ni neighbour (green squares). Such configurations indicate extra freedom of the

atomic arrangements with the same chemical composition.

The hardness of the alloy as a function of annealing time at 200 °C and 300 °C is given in Fig. 3(a), with the corresponding change in the spacing of the IMC fibres during the annealing being shown in Fig. 3(b). There is a slight decrement in hardness after annealing at 200 °C and the hardness decreases very quickly after annealing at 300 °C. The spacing of the IMC fibres increases from 98 ± 32 nm at the as-cast state to 122 ± 25 nm after annealing at 200 °C for 360 h, and further to 160 ± 25 nm after annealing at 300 °C for 360 h, indicating the excellent thermal stability of the IMC phase. The eutectic microstructure after annealing is shown in Fig. 3(c)–(f), where little change in eutectic Si and IMC can be seen after annealing at 200 °C for different times. However, coarsening of eutectic Si takes place after annealing at 300 °C as shown in Fig. 3(e) and (f). The diameters of eutectic Si are 100–300 nm after annealing at 300 °C for 360 h. The coarsening of the eutectic Si seems to be the main cause of the decrease in hardness after annealing at 300 °C.
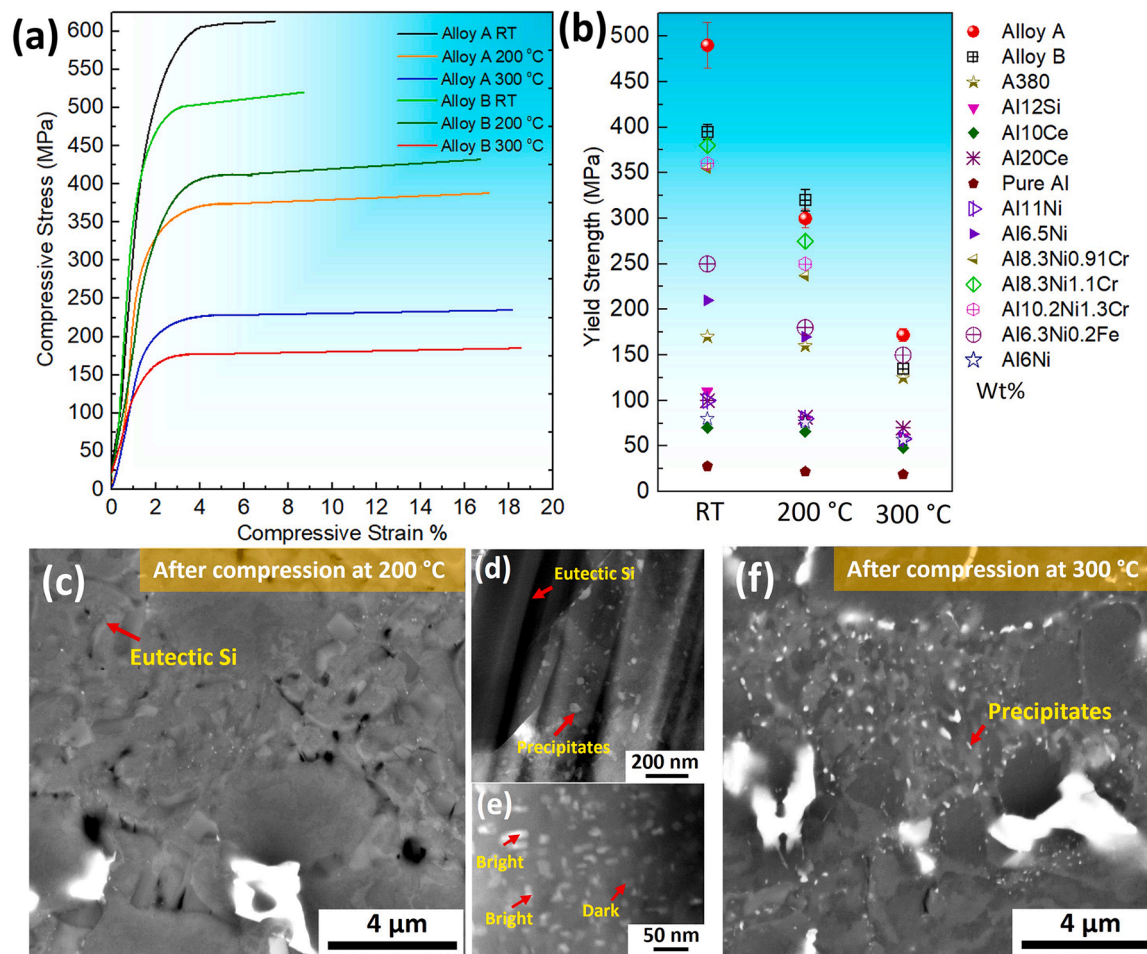
Fig. 4. (a) Room-temperature (RT) and elevated-temperature compressive curves of Alloy A and Alloy B (b) yield strength versus temperature of Alloy A, Alloy B and some other aluminium alloys; microstructure of Alloy B after compression test at 200 °C (c) SEM backscattered image of eutectic region, HAADF-STEM image of precipitates in α-Al under low magnification (d) and high magnification (e); (f) SEM backscattered image of eutectic region in Alloy B after compression test at 300 °C.

Figure 4(a) shows the compressive stress-strain curves of Alloy A and Alloy B from room temperature (RT) to 300 °C. Alloy A has a yield strength of 485 ± 20 MPa at RT. Compared with Alloy A, Alloy B has a much lower yield strength of 396 ± 10 MPa. At 200 °C, Alloy B has a slightly higher yield strength of 320 ± 12 MPa than Alloy A, which has a yield strength of 300 ± 10 MPa. At 300 °C, Alloy A and Alloy B have yield strengths of 172 ± 7 MPa and 135 ± 6 MPa, respectively. Alloy A exhibits a much higher yield strength at 300 °C. The compressive yield strengths of Alloy A, Alloy B and some other heat-resistant aluminium alloys from RT to 300 °C are summarised in Fig. 4(b). It can be found that Alloy A has very competitive mechanical properties, which is very potential for industrial applications.

Alloy B has a coarser microstructure than Alloy A. In Alloy B, the eutectic Si has a diameter of 300–700 nm and coarse lamellar/granular IMCs have a micro-scale size. Thus, Alloy A with nano-scale eutectic microstructure has a much higher yield strength than Alloy B. However, Alloy A has a slightly lower yield strength than Alloy B at 200 °C. It is because of precipitation hardening of Alloy B at 200 °C. Because of rapid cooling, a supersaturation of Cu and Mg is obtained [31,32]. Thus, after soaking or during compression test at 200 °C, numerous nano-scale precipitates can form which contributes to the strength of the alloy. As a result, less sacrifice of strength takes place. As shown in the HAADF-STEM image from Fig. 4(d) and (e), bright phases are θ/θ' (Al₂Cu) phase [20,33] and dark phases are Q/Q' phase [15,16,20,34], which formed in α-Al matrix after the compression test at 200 °C. At 300 °C, Alloy A has a much higher strength than Alloy B. The

Table 1
Eutectic microstructure and yield strength in different heat-resistant eutectic alloys.

Alloy composition/ wt%	Casting method	Microstructure (inter-lamellar/rod spacing)	Volume fraction (phase)/%	Yield Strength/ MPa	
				200 °C	300 °C
Al-10Ce [36]	Steel mould	α-Al+A₁₁Ce₃ (0.5–1 μm)	10% (Al₁₁Ce₃)	66	48
Al-6Ni [37]	∅32 × 127 mm	α-Al+Al₃Ni (1.7 μm)	14.2% (Al₃Ni)	76	57
Al-6.5Ni [38]	Copper mould	α-Al+Al₃Ni (370 nm)	–	170 ± 11	–
Al-8.3Ni-0.91Cr [38]	∅3 mm	α-Al+Al₃Ni (250–350 nm)	–	237 ± 14	–
Al-8.3Ni-1.1Cr [38]		α-Al+Al₃Ni (150–200 nm)	–	275 ± 10	–
Al-10.2Ni-1.3Cr [38]		α-Al+Al₃Ni (200–270 nm)	–	250 ± 8	–
Al-6.3Ni-0.2Fe [39]		α-Al+Al₃Ni/ Al₉FeNi (90–140 nm)	–	180 ± 12	150 ± 15
Al-15.0Si-4.1Ni-1.9Fe (Current work)	Copper mould ∅5 mm	α-Al+Si+IMC (98–140 nm)	14.3 ± 1.6%(Si), 15.1 ± 1.9%(IMC)	300 ± 10	172 ± 7

microstructure of Alloy B after compression at 300 °C is displayed in Fig. 4(f). Compared with the microstructure in Fig. 4(c) under the same magnification, it can be found that a large number of bright precipitates (θ/θ' phase) are visible under SEM. These precipitates are much coarser than that after compression at 200 °C (Fig.4(d) and (e)), due to Ostwald ripening process [35,19]. At 300 °C, these coarsening precipitates made a limited contribution to strength in Alloy B. However, the main strengthening phases in Alloy A at 300 °C are short-fibrous ultrafine IMCs, which contributes to the high strength of the alloy. Furthermore, the mechanical properties of eutectic composites mainly depend on the types, volume fraction, morphology and size of eutectic phases. The detailed microstructure and yield strength of some other heat-resistant eutectic alloys are summarised in Table 1. It can be found that a higher volume fraction and refinement of IMCs leads to a higher strength at elevated temperatures. The additional elements in binary eutectic systems or multicomponent eutectic solidification can lead to refined microstructure, which is favourable for the mechanical properties.

In conclusion, the microstructure and compressive mechanical properties of Al-15.0Si-4.1Ni-1.9Fe (wt%) alloy with ternary eutectic solidification (Liquid→α-Al+Si+(Al,Si)$_5$(Fe,Ni)) was studied. The (Al,Si)$_5$(Fe,Ni) phase with a volume fraction of $15.1 \pm 1.9\%$ is a tetragonal Al$_{2.7}$FeSi$_{2.3}$-type phase and plays an important role in the mechanical properties at room and elevated temperatures. The alloy shows higher mechanical properties at room temperature and 300 °C compared with Al-12.8Si-3.9Cu-1.9Ni-1.0Mg-0.4Fe (wt%) alloy and some other typical aluminium alloys. It has great potential for application in the industry for elevated-temperature applications.

Declaration of Interest Statement

The authors declare that they have no known competing financial interests or personal relationships that could have appeared to influence the work reported in this paper.

Acknowledgments

Supplementary materials

Supplementary material associated with this article can be found, in the online version, at doi:10.1016/j.scriptamat.2023.115707.

References

[1] F. Czerwinski, Thermal stability of aluminum alloys, Materials (Basel) 13 (2020) 1–49, https://doi.org/10.3390/ma13153441.

[2] F. Czerwinski, Critical assessment 40: a search for the eutectic system of high-temperature cast aluminium alloys, Mater. Sci. Technol. 37 (2021) 683–692, https://doi.org/10.1080/02670836.2021.1940670.

[3] L. Kerni, A. Raina, M.I.U. Haq, Performance evaluation of aluminium alloys for piston and cylinder applications, Mater. Today Proc. 5 (2018) 18170–18175, https://doi.org/10.1016/j.matpr.2018.06.153.

[4] M. Akhtar, S.Z. Qamar, M. Muhammad, A. Nadeem, Optimum heat treatment of aluminum alloy used in manufacturing of automotive piston components, Mater. Manuf. Process. 33 (2018) 1874–1880, https://doi.org/10.1080/10426914.2018.1512128.

[5] T. Liu, A. Li, C. Zhu, W. Yuan, Effect of alloying elements on surface temperature field of aluminum piston in diesel engine, Eng. Fail. Anal. 134 (2022), 106020, https://doi.org/10.1016/j.engfailanal.2021.106020.

[6] A. Ahmed, M.S. Wahab, A.A. Raus, K. Kamarudin, Q. Bakhsh, D. Ali, Mechanical properties, material and design of the automobile piston: an ample review, Indian J. Sci. Technol. 9 (2016), https://doi.org/10.17485/ijst/2016/v9i36/102155.

[7] N.A. Belov, D.G. Eskin, N.N. Avxentieva, Constituent phase diagrams of the Al-Cu-Fe-Mg-Ni-Si system and their application to the analysis of aluminium piston alloys, Acta Mater. 53 (2005) 4709–4722, https://doi.org/10.1016/j.actamat.2005.07.003.

[8] J.J. Tang, C. Liang, C.G. Xu, Effects of alloying elements and temperature on thermodynamic state and microstructure of piston aluminum alloy, Defect Diffus. Forum 417 (2022) 3–8, https://doi.org/10.4028/p-1421c8.

[9] M. Warmuzek, Chemical composition of the Ni-containing intermetallic phases in the multicomponent Al alloys, J. Alloys Compd. 604 (2014) 245–252, https://doi.org/10.1016/j.jallcom.2014.03.119.

[10] K. Bugelnig, F. Sket, H. Germann, T. Steffens, R. Koos, F. Wilde, E. Boller, G. Requena, Influence of 3D connectivity of rigid phases on damage evolution during tensile deformation of an AlSi12Cu4Ni2 piston alloy, Mater. Sci. Eng. A 709 (2018) 193–202, https://doi.org/10.1016/j.msea.2017.10.035.

[11] C.L. Chen, R.C. Thomson, The combined use of EBSD and EDX analyses for the identification of complex intermetallic phases in multicomponent Al-Si piston alloys, J. Alloys Compd. 490 (2010) 293–300, https://doi.org/10.1016/j.jallcom.2009.09.181.

[12] D.G. Eskin, Decomposition of supersaturated solid solutions in Al–Cu–Mg–Si alloys, J. Mater. Sci. 38 (2003) 279–290, https://doi.org/10.1023/A:1021109514892.

[13] L. Gao, X. Ou, S. Ni, K. Li, Y. Du, M. Song, Effects of θ′ precipitates on the mechanical performance and fracture behavior of an Al–Cu alloy subjected to overaged condition, Mater. Sci. Eng. A. 762 (2019), 138091, https://doi.org/10.1016/j.msea.2019.138091.

[14] M. Yang, H. Chen, A. Orekhov, Q. Lu, X. Lan, K. Li, S. Zhang, M. Song, Y. Kong, D. Schryvers, Y. Du, Quantified contribution of β″ and β′ precipitates to the strengthening of an aged Al–Mg–Si alloy, Mater. Sci. Eng. A 774 (2020), 138776, https://doi.org/10.1016/j.msea.2019.138776.

[15] L. Zuo, B. Ye, J. Feng, X. Kong, H. Jiang, W. Ding, Effect of Q-Al5Cu2Mg8Si6 phase on mechanical properties of Al-Si-Cu-Mg alloy at elevated temperature, Mater. Sci. Eng. A. 693 (2017) 26–32, https://doi.org/10.1016/j.msea.2017.03.087.

[16] X. Zhu, X. Dong, P. Blake, S. Ji, Improvement in as-cast strength of high pressure die-cast Al–Si–Cu–Mg alloys by synergistic effect of Q-Al5Cu2Mg8Si6 and θ-Al2Cu phases, Mater. Sci. Eng. A. 802 (2021), 140612, https://doi.org/10.1016/j.msea.2020.140612.

[17] Y. Sui, D. Ji, L. Han, Q. Wang, Characterization of the aging precipitates of Al-12Si-4Cu-2Ni-0.8Mg-0.2Gd piston alloy, JOM 71 (2019) 366–372, https://doi.org/10.1007/s11837-018-3080-0.

[18] Y.F. Song, X.F. Ding, L.R. Xiao, X.J. Zhao, Z.Y. Cai, L. Guo, Y.W. Li, Z.Z. Zheng, Effects of two-stage aging on the dimensional stability of Al-Cu-Mg alloy, J. Alloys Compd. 701 (2017) 508–514, https://doi.org/10.1016/j.jallcom.2017.01.139.

[19] J. Rakhmonov, K. Liu, G.X. Chen, Effects of compositional variation on the thermal stability of θ′-Al2Cu precipitates and elevated-temperature strengths in Al-Cu 206 alloys, J. Mater. Eng. Perform. 29 (2020) 7221–7230, https://doi.org/10.1007/s11665-020-05227-5.

[20] H.Q. Liu, J.C. Pang, M. Wang, S.X. Li, Z.F. Zhang, Effect of temperature on the mechanical properties of Al–Si–Cu–Mg–Ni–Ce alloy, Mater. Sci. Eng. A (2021) 824, https://doi.org/10.1016/j.msea.2021.141762.

[21] L. Zuo, B. Ye, J. Feng, H. Zhang, X. Kong, H. Jiang, Effect of ε-Al3Ni phase on mechanical properties of Al–Si–Cu–Mg–Ni alloys at elevated temperature, Mater. Sci. Eng. A 772 (2020), 138794, https://doi.org/10.1016/j.msea.2019.138794.

[22] M.S. Jo, Y.H. Cho, J.M. Lee, S.H. Kim, J.Y. Kang, J.G. Jung, S.B. Kim, J. il Jang, A new Zr-rich intermetallic phase in an Al-14Si-3Cu-4.5Ni casting alloy with trace additions of Zr, Intermetallics 117 (2020), 106667, https://doi.org/10.1016/j.intermet.2019.106667.

[23] B. Cantor, Multicomponent high-entropy Cantor alloys, Prog. Mater. Sci. 120 (2021), 100754, https://doi.org/10.1016/j.pmatsci.2020.100754.

[24] J.-W.J.W. Yeh, S.-K.S.K. Chen, S.-J.S.J. Lin, J.-Y.J.Y. Gan, T.-S.T.S. Chin, T.T.T.-T. Shun, C.H.C.-H. Tsau, S.Y.S.-Y. Chang, Nanostructured high-entropy alloys with multiple principal elements: novel alloy design concepts and outcomes, Adv. Eng. Mater. 6 (2004) 299–303, https://doi.org/10.1002/adem.200300567.

[25] U. Böyük, Physical and mechanical properties of Al-Si-Ni eutectic alloy, Met. Mater. Int. 18 (2012) 933–938, https://doi.org/10.1007/s12540-012-6004-5.

[26] C.S. Tiwary, P. Pandey, S. Sarkar, R. Das, S. Samal, K. Biswas, K. Chattopadhyay, Five decades of research on the development of eutectic as engineering materials, Prog. Mater. Sci. 123 (2022), 100793, https://doi.org/10.1016/j.pmatsci.2021.100793.

[27] B.J. Kim, A.K. Dahle, Y.H. Park, Y.C. Lee, The effect of Sr additions on Al–Cu–Si ternary eutectic alloys for a high-ductility bimodal microstructure, Mater. Sci. Eng. A 833 (2022), 142547, https://doi.org/10.1016/j.msea.2021.142547.

[28] Q. Cai, C.L. Mendis, I.T.H. Chang, Z. Fan, Microstructure and mechanical properties of new die-cast quaternary Al-Cu-Si-Mg alloys, Mater. Sci. Eng. A 800 (2021), 140357, https://doi.org/10.1016/j.msea.2020.140357.

[29] Y. Yang, K. Yu, Y. Li, D. Zhao, X. Liu, Evolution of nickel-rich phases in Al-Si-Cu-Ni-Mg piston alloys with different Cu additions, Mater. Des. 33 (2012) 220–225, https://doi.org/10.1016/j.matdes.2011.06.058.

[30] C. Gueneau, C. Servant, F. D'Yvoire, N. Rodier, FeAl3Si2, Acta Crystallogr. Sect. C Cryst. Struct. Commun. 51 (1995) 177–179, https://doi.org/10.1107/S0108270194009030.

[31] E.J. Lavernia, J.D. Ayers, T.S. Srivatsan, Rapid solidification processing with specific application to aluminium alloys, Int. Mater. Rev. 37 (1992) 1–44, https://doi.org/10.1179/imr.1992.37.1.1.

[32] I. Lichioiu, I. Peter, B. Varga, M. Rosso, Preparation and structural characterization of rapidly solidified Al–Cu alloys, J. Mater. Sci. Technol. 30 (2014) 394–400, https://doi.org/10.1016/j.jmst.2013.12.001.

[33] B.K. Milligan, S. Roy, C.S. Hawkins, L.F. Allard, A. Shyam, Impact of microstructural stability on the creep behavior of cast Al–Cu alloys, Mater. Sci. Eng. A 772 (2020), 138697, https://doi.org/10.1016/j.msea.2019.138697.

[34] A.R. Farkoosh, M. Pekguleryuz, Enhanced mechanical properties of an Al-Si-Cu-Mg alloy at 300 °C: effects of Mg and the Q-precipitate phase, Mater. Sci. Eng. A 621 (2015) 277–286, https://doi.org/10.1016/j.msea.2014.10.080.

[35] H. Xiao, K. Zhang, C. Shi, Z. Lu, J. Jiang, Influence of electropulsing treatment combined with pre-deformation on ageing behavior and mechanical properties of 5A90 Al-Li alloy, J. Alloys Compd. 784 (2019) 1234–1247, https://doi.org/10.1016/j.jallcom.2019.01.103.

[36] F. Czerwinski, Thermal stability of aluminum–cerium binary alloys containing the Al–Al11Ce3 eutectic, Mater. Sci. Eng. A. 809 (2021), 140973, https://doi.org/10.1016/j.msea.2021.140973.

[37] F. Czerwinski, Thermal stability of aluminum-nickel binary alloys containing the Al-Al3Ni eutectic, Metall. Mater. Trans. A 52 (2021) 4342–4356, https://doi.org/10.1007/s11661-021-06372-9.

[38] P. Pandey, S. Kashyap, C.S. Tiwary, K. Chattopadhyay, Development of high-strength high-temperature cast Al-Ni-Cr alloys through evolution of a novel composite eutectic structure, Metall. Mater. Trans. A Phys. Metall. Mater. Sci. 48 (2017) 5940–5950, https://doi.org/10.1007/s11661-017-4369-2.

[39] C.S. Tiwary, S. Kashyap, D.H. Kim, K. Chattopadhyay, Al based ultra-fine eutectic with high room temperature plasticity and elevated temperature strength, Mater. Sci. Eng. A. 639 (2015) 359–369, https://doi.org/10.1016/j.msea.2015.05.024.